Numerical Simulation of the Evolution of a Gas Bubble in a Liquid Near a Wall

A. A. Aganin*, L. A. Kosolapova, and V. G. Malakhov

Institute of Mechanics and Engineering, Kazan Science Center, Russian Academy of Sciences (IME KazSC RAS), Kazan, Russia
e-mail: aganin54@mail.ru

Abstract—A numerical technique based on the application of the boundary element method is proposed for studying the axially symmetric dynamics of a bubble in a liquid near a solid wall. It is assumed that the liquid is ideally incompressible and its flow is potential. The process of expansion and contraction of a spheroidal bubble is considered, including the toroidal phase of its movement. The velocity and pressure fields in the liquid surrounding the bubble are evaluated along with the shape of the bubble surface and the velocity of its displacement. The numerical convergence of the algorithm with an increase in the number of boundary elements and a refinement of the time step is shown, and comparison with the experimental and numerical results of other authors is performed. The capabilities of the technique are illustrated by solving a problem of collapse of a spheroidal bubble in water. The bublle is located a short distance from the wall.

1. INTRODUCTION

Studying the dynamics of bubbles near a wall is important for understanding the impact of cavitation on the surface of solid bodies. Despite the existence of analytical dependences for estimating such an impact [1], the complexity of the phenomenon requires applying more precise models for describing it and effective numerical approaches. Using the method of finite differences, work [2] was the first to describe the formation of a cumulative liquid jet on the surface of a bubble directed towards the surface of a wall, which was predicted in [3]. Such jets are considered the main mechanisms of cavitation erosion.

Currently, the dynamics of bubbles near a wall are studied using various numerical methods [4–6]. The most widespread numerical techniques for regimes with a small influence of the compressibility and viscosity of liquid are the ones based on the boundary element method (BEM), which reduces the boundary problem for the Laplace equation for the potential of liquid velocity to an integral equation along the domain boundary. Work [7] proposes the numerical approach based on BEM, which was later applied in [8] to investigate the axisymmetric deformation of an empty spheroidal cavity near a solid wall. For application to problems of the axisymmetric dynamics of a bubble, BEM was developed in [9] where it was generalized to the case of the dynamics of a vapor bubble in a liquid flux moving at a given velocity. In [10, 11] BEM was adapted to spatial problems of bubble dynamics.

In those and some other works, computations were continued until the moment when the cumulative jet hit the opposite side of the bubble surface. The next step in developing a technique using BEM was its extension to the toroidal phase of motion, which causes the circulation of a liquid flow around a doubly connected domain of a bubble [12–17]. In order to account for flow rotation a cut is introduced within the jet in [12], representing a moving material surface and connecting the symmetry axis with the bubble surface. This cut makes the jet domain simply connected and allows one to use BEM in the same way as before the moment of impact. In [13] a similar approach is used without the assumption [12] about the constancy of the potential jump along the cut. In [15] the flow rotation is accounted for by representing the velocity potential as the sum of the potentials of a vortex ring and unambiguously defined residual potential, which satisfies the Laplace equation and is determined by BEM.

This work presents a realization of the numerical technique for investigating the evolution of a bubble near a wall based on the approach described in [17] and representing a simplified methodology [12]. The

rotation of a liquid flow is taken into consideration by the introduction of an artificial flat cut perpendicular to the symmetry axis. In contrast to the authors of other works [15, 18], we use a smoothing cubical spline in order to eliminate the numerical instability appearing during the realization of the methodology. Before the moment of the formation of a toroidal bubble, the technique of this work follows the algorithm realized by the authors in [19]. The main results obtained using this algorithm are described in [19–21]. They are devoted to studying the influence of the initial nonsphericity of the bubble and the initial distance from the bubble to the wall during the process of its collapse, as well as the dynamics of two bubbles appearing during the collapse of a flattened spheroidal bubble.

The possibilities of the technique described in this work are demonstrated on the problem about the expansion and the subsequent contraction of a spheroidal bubble near a wall.

2. PROBLEM STATEMENT

The axisymmetric dynamics of a cavitation bubble in a liquid near a solid wall is studied. It is assumed that the liquid surrounding the bubble is ideal and incompressible; and its motion is potential and is described by the equations

$$\Delta\Phi = 0, \tag{1}$$

$$\Phi_t + \frac{1}{2}(\nabla\Phi)^2 + \frac{p - p_\infty}{\rho_f} = 0, \tag{2}$$

where t is time, p and p_∞ are the liquid pressure at an arbitrary point and at infinity, ρ_f is the liquid density, and Φ is the velocity potential.

It is assumed that vapor in a cavitation bubble behaves as a van der Waals gas with uniform pressure distribution

$$p^- = p_b^0 X, \quad X = (1 + \bar{a})\left(\frac{1 - \bar{b}}{V/V_0 - \bar{b}}\right)^\kappa - \bar{a}\left(\frac{V_0}{V}\right)^2, \tag{3}$$

where $\bar{a} = a/(V_0^2 p_b^0), \bar{b} = b/V_0$, p_b^0 is the initial gas pressure in the bubble, V_0 and V are the initial and current volumes of the bubble, κ is the adiabatic exponent, and a and b are gas constants.

The dynamic

$$p^+ = p^- - 2\sigma H \tag{4}$$

and kinematic

$$d\bar{x}/dt = \bar{v} \tag{5}$$

boundary conditions are fulfilled on the surface of the bubble. In (4) and (5) p^+ is the pressure on the liquid side of the surface, σ is the surface tension coefficient, H is the average curvature at a point of the bubble surface, and $\bar{x}, \bar{v} = (\nabla\Phi)$ are the radius-vector and velocity of the surface point.

The impermeability condition is posed on a solid wall as

$$v_z = \partial\Phi/\partial z = 0, \tag{6}$$

where z is the coordinate along the rotation axis.

3. NUMERICAL SOLUTION METHOD

The evolution of a bubble can be split into two phases (Fig. 1). The first one corresponds to the formation of a cumulative jet on the bubble surface. It ends at the moment t_c, when the jet hits part of bubble surface nearest the wall. The second phase corresponds to the motion of a toroidal bubble formed as a result of this impact. Taking this into account, the algorithm of the numerical solution is split into two steps, corresponding to the computation of the first and second phases of the bubble's dynamics.

The motion and deformation of the bubble surface in time are defined by a step-by-step method based on the kinematic and dynamic boundary conditions (4) and (5); the liquid's velocity in the profile and the velocity potential at some moment of time are computed using BEM.
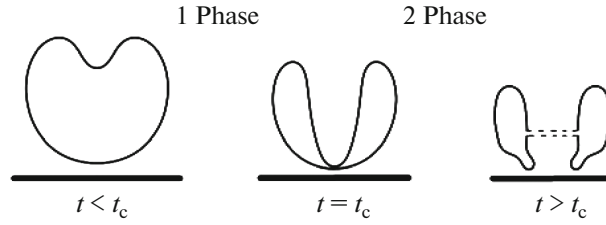
1 Phase   2 Phase

$t < t_c$ $t = t_c$ $t > t_c$

Fig. 1.

At the first phase of motion, the velocity potential Φ and its normal derivative $\partial\Phi/\partial n$ on the surface are connected by the boundary integral equation (BIE) [22]

$$c(x)\Phi(x) = \int_S \left(G(x,y)\frac{\partial\Phi(y)}{\partial n} - \Phi(y)\frac{\partial G(x,y)}{\partial n}\right)dS(y), \tag{7}$$

where $x, y \in S$ are the points of observation and integration, $\bar{n}$ is the vector of the normal directed inside the bubble, $G(x, y)$ is the fundamental solution (Green's function), which is denoted as follows for a half-space in Neumann's condition:

$$G(x,y) = \frac{1}{4\pi}\left(\frac{1}{r} + \frac{1}{r^*}\right). \tag{8}$$

In (8) $r = |x - y|$ is the distance between points x and y and $r^* = |x^* - y|$ is the distance between point x^*, symmetrical to point x relative to the wall, and point y. Parameter $c(x)$ in (7) is assumed to be 0.5 in the case of a smooth boundary at point x, and $\beta/(2\pi)$, for an angular point of boundary x with angle β at the vertex. For known values of potential Φ on the surface S, BIE (7) allows defining the values of the normal derivative $\partial\Phi/\partial n$.

For an axisymmetric problem, Eq. (7) in a cylindrically symmetric coordinate system will be denoted as

$$c(\rho,z)\Phi(\rho,z) = \int_L \left\{\psi(\rho_0,z_0)K_1(\rho_0,z_0,\rho,z,t) - \Phi(\rho_0,z_0)K_2(\rho_0,z_0,\rho,z,t)\right\}ds_0, \tag{9}$$

where

$$\psi(\rho_0,z_0) = \frac{\partial\Phi(\rho_0,z_0)}{\partial n_0}, \quad K_1(\rho_0,z_0,\rho,z,t) = \frac{\rho_0}{\pi}\left(\frac{K(m)}{A} + \frac{K(m_2)}{A_2}\right),$$

$$K_2(\rho_0,z_0,\rho,z,t) = \frac{1}{\pi}\left[-\frac{1}{2}\left(\frac{K(m)}{A} + \frac{K(m_2)}{A_2}\right)\frac{dz_0}{ds_0}\right.$$

$$+ \left(\frac{1}{2}\frac{dz_0}{ds_0} + \frac{\rho_0}{d^2}\left((\rho - \rho_0)\frac{dz_0}{ds_0} - (z - z_0)\frac{d\rho_0}{ds_0}\right)\right)\frac{E(m)}{A}$$

$$\left.+ \left(\frac{1}{2}\frac{dz_0}{ds_0} + \frac{\rho_0}{d_2^2}\left((\rho - \rho_0)\frac{dz_0}{ds_0} + (z + z_0)\frac{d\rho_0}{ds_0}\right)\right)\frac{E(m_2)}{A_2}\right],$$

(ρ, z) are the coordinates of the observation point x, (ρ_0, z_0) are the coordinates of the integration point y, and s_0 is the angular coordinate of the profile,

$$A = \left[(\rho + \rho_0)^2 + (z - z_0)^2\right]^{1/2}, \quad d = \left[(\rho - \rho_0)^2 + (z - z_0)^2\right]^{1/2},$$

$$A_2 = \left[(\rho + \rho_0)^2 + (z + z_0)^2\right]^{1/2}, \quad d_2 = \left[(\rho - \rho_0)^2 + (z + z_0)^2\right]^{1/2},$$

$$m = 2\sqrt{\rho\rho_0}/A, \quad m_2 = 2\sqrt{\rho\rho_0}/A_2,$$

$$K(m) = \int_0^{\pi/2}\frac{d\theta}{\sqrt{1 - m^2\sin^2\theta}}, \quad E(m) = \int_0^{\pi/2}\sqrt{1 - m^2\sin^2\theta}\,d\theta, \quad 0 \le m \le 1,$$

and $K(m)$ and $E(m)$ are the complete elliptic integrals of type I and II.

Equations (9) are solved using BEM. At the same time, the bubble surface profile is approximated by a polygonal line consisting of N elements. Within the limits of an element, functions $\psi(\rho_0, z_0)$ and $\Phi(\rho_0, z_0)$ are assumed to be linear.

The algorithm for solving problem (1)−(6) is realized as follows. Assume that at the moment $t^{(m)}$, the geometry of the bubble profile, the distribution of potential $\Phi^{(m)}$ on it, and the pressure in the bubble are known.

1. At the profile points, derivative $\partial\Phi/\partial s$ is computed by the values of the potential on the profile.

2. $\partial\Phi/\partial n$ on profile at the moment $t^{(m)}$ is defined from the solution of BIE.

3. The radial v_ρ and axial v_z components of velocity are computed by $\partial\Phi/\partial s$ and $\partial\Phi/\partial n$, taking the expressions for the components of the normal $n_\rho = z_s$ and $n_z = -\rho_s$ into account:

$$v_\rho = \frac{\partial\Phi}{\partial\rho} = \frac{\partial\Phi}{\partial s}\rho_s + \frac{\partial\Phi}{\partial n}z_s, \quad v_z = \frac{\partial\Phi}{\partial z} = \frac{\partial\Phi}{\partial s}z_s - \frac{\partial\Phi}{\partial n}\rho_s.$$

4. The position of the profile points at the moment $t^{(m+1)} = t^{(m)} + \tau^{(m)}$ is defined by the formulas

$$\rho^{(m+1)} = \rho^{(m)} + \tau^{(m)}\partial\Phi^{(m)}\big/\partial\rho, \quad z^{(m+1)} = z^{(m)} + \tau^{(m)}\partial\Phi^{(m)}\big/\partial z.$$

5. The new volume of the bubble at the moment $t^{(m+1)}$ is determined and the current pressure in it is computed from condition (3).

6. The value of the potential on the new profile is computed for $t^{(m+1)}$:

$$\Phi^{(m+1)} \approx \Phi^{(m)} + \frac{D\Phi}{Dt}\tau^{(m)} = \Phi^{(m)} + \tau^{(m)}\left(\frac{\partial\Phi}{\partial t} + (\nabla\Phi)^2\right)^{(m)}.$$

Derivative $\partial\Phi\big/\partial t$ is defined using the Cauchy-Lagrange integral (2) on the bubble surface at the moment $t^{(m)}$, taking the dynamic condition (4) and the adiabatic law of the change in pressure (3) into account.

The stability of the algorithm is provided by condition [23]

$$\tau^{(m)} = a\sqrt{\frac{\rho_f}{p_\infty}}C\left(1 + 0.5\frac{\rho_f}{p_\infty}v_{\max}^2 + \frac{p_b^0}{p_\infty}X + \frac{2\sigma}{p_\infty}|H|_{\max}\right)^{-1}, \quad m = 0, 1, ..., \tag{10}$$

where a is the maximal linear size of a bubble, $v_{\max}$ and $|H|_{\max}$ are the maximal values of v and H on the profile, and C is the dimensionless parameter, usually $0.001 < C < 0.02$, defined by the numerical experiment.

After defining the position of the profile and distribution of the potential on it, the computation pass to point 1. For the initial moment $t^{(0)}$ it is taken that $\Phi^{(0)} = 0$.

Instability in the form of "sawtooth" high-frequency distortions of the profile shape may take place during the realization of the described step-by-step algorithm. In this work we suggest a way to smoothen the distortions using a cubical spline, when the function f set by its values f_k at the partitioning nodes of its changing interval is approximated by spline S_3, which is a solution of the variation problem

$$\int_{s_1}^{s_{N+1}} (S_3''(s))^2 dx + \sum_{k=1}^{N+1}\frac{1}{w_k}(S_3(s_k) - f_k)^2 \to \min, \tag{11}$$

where w_k are the settable weight coefficients. Spline S_3 is defined unambiguously by setting two boundary conditions on the ends of the interval. The splines are built at each time step in order to smoothen functions $\rho(s)$, $z(s)$, and $\Phi(s)$ using the boundary conditions

$$\rho'(s_1) = 1, \quad \rho'(s_{N+1}) = -1, \quad z'(s_1) = 0, \quad z'(s_{N+1}) = 0, \quad \Phi'(s_1) = 0, \quad \Phi'(s_{N+1}) = 0. \tag{12}$$

Note that for excessively large values of the smoothening parameters w_i in (11), the numerical solution of the problem may turn out to be significantly distorted. Thus, computation is performed by decreasing values w_i until solutions for two sequential sets of w_i are sufficiently close. The computations show that we

should select values w_i from the interval $10^{-10} \leq w_i/V_{max} \leq 10^{-6}$, where V_{max} is the maximal volume of the bubble.

Application of the described algorithm may lead to a strong nonuniformity of the distribution of the profile's partitioning grid nodes. This defect can be eliminated by periodically restructuring the net.

A toroidal bubble is formed at the initial moment of the second motion phase as a result of the impact of the jet. The method of the numerical transition from a simply connected to a doubly connected toroidal bubble surface is described in [17]. At the same time, the velocity potential is defined ambiguously. In order to eliminate this ambiguousness, it is necessary to introduce an infinitely thin linear cut perpendicular to the symmetry axis that connects any point of the torus cross section with the axis (Fig. 1, the cut is shown by the dashed lines on the right). It is assumed that the velocity potential along the cut is subjected to a discontinuity, whose value is constant along the cut and equals the difference $\Delta\Phi$ of the potentials of the end of the jet and a point on the symmetry axis on the opposite side of the bubble surface. The value $\Delta\Phi$ is defined by these values at the end of the first motion phase. In this way, the flow domain again becomes simply connected and the methodology used in the first motion phase of bubble is applied in the second phase, with the difference that a new term appears in BEI, containing an integral over the cut. At that, the integral equation takes the form [17]

$$c(x)\Phi(x) = \int_S \left(G(x,y)\frac{\partial\Phi(y)}{\partial n} - \Phi(y)\frac{\partial G(x,y)}{\partial n} \right) dS(y) - \Delta\Phi \int_{T^+} \frac{\partial G(x,y)}{\partial n} ds(y), \tag{13}$$

where S is the toroidal surface apart from the cut and T^+ is the upper surface of the cut. Since the normal at the point of intersection of the profile and the cut is undefined, then integral equation (13) in it is not used and the derivative along the normal $\partial\Phi/\partial n$ at this point is defined by linear interpolation through the values at the two neighboring points of a discrete profile partition. At that, the interpolation formula closes the set of linear equations defining the values of $\partial\Phi/\partial n$ at the profile points.

The position of the cut at each time step can be selected arbitrarily. In this work, the cut was selected at the level $z = z_c$, where z_c is the axial coordinate of the gravity center of a toroidal bubble. Then the position of the cut was not changed on z if the displacement of the gravity center of the torus cross section in the following steps did not exceed 1/16 of its size along the rotation axis. For larger displacements of the gravity center along the symmetry axis, the position of the cut is changed. At that, the values of the potential on the profile are redefined by the addition or subtraction of $\Delta\Phi$ so that the potential jump would occur on the new position of the cut.

Similarly to the first motion phase of the bubble, smoothening is here applied to functions $\rho(s)$, $z(s)$, and $\Phi(s)$ using a spline, where instead of conditions (12), functions $\rho(s)$ and $z(s)$ are subjected to periodicity conditions while $\Phi(s)$ are subjected to $\Phi''(s_1) = 0$, $\Phi''(s_{N+1}) = 0$.

The numerical technique also includes computing fields of velocity and pressure in the liquid surrounding the bubble. At that, potential Φ is determined by Eqs. (7) or (13), where $c = 1$. The velocity components are computed using finite difference formulas of the second order of accuracy. The pressure in the liquid is computed by Eq. (2), where $\partial\Phi/\partial t$ is also defined by the finite difference formulas.

The results are described using the dimensionless quantities

$$R^* = R_0/R_m, \quad \gamma = d/R_m, \quad \rho^* = \rho/R_m, \quad z^* = z/R_m, \quad t^* = t/\left(R_m\sqrt{\rho_f/p_\infty}\right),$$

where R_0 is the initial radius of the bubble, d is the distance from its center to the wall, and R_m is the maximal radius of the bubble achieved during its spherical expansion without taking the wall into account.

4. TESTING

4.1. The "practical convergence" of the algorithm was studied on the solution of the problem on the contraction of a slightly flattened spheroidal bubble in water which is in contact with a wall. The ratio of the spheroid's semiaxes $e = 0.9$ and the initial bubble volume equals that of a sphere of radius $R_0 = 1$ mm. The pressure at "infinity" is constant: $p_\infty = 1$ bar. The pressure of the vapor in the bubble at the beginning of contraction p_b^0 equals the saturation pressure for water at room temperature.

For the first phase of the motion, where the bubble remains simply connected, Fig. 2 shows the results of the numerical experiments performed for different numbers of the bubble profile's partitioning elements N and various values of parameter C in (10), which characterizes the initial time step. The dependences of the velocity of the cumulative jet end on time are presented for various values of N (Fig. 2a), as well as the dependences of the relative error of fulfillment of the condition of total energy constancy
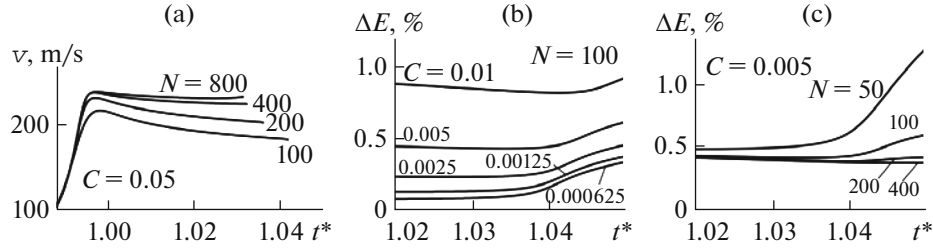
Fig. 2. (a) Dependence of jet end velocity on time for different number of bubble profile partitions N; (b) integral computation error depending on parameter C for $N = 100$; (c) integral energy computation error depending on N for $C = 0.005$.

$\Delta E = (E_k + E_p)/\max_t E_k$ on C (Fig. 2b) and N (Fig. 2c). Here E_k and E_p are the kinetic and potential energies

$$E_k = \frac{\rho_f}{2} \int_S \Phi \frac{\partial \Phi}{\partial n} ds, \quad E_p = p_\infty (V - V_0) - p_b^0 \int_{V_0}^{V} X dV.$$

For zero initial velocity, ΔE must be zero in the considered time interval. It can be seen that convergence by the velocity at the end of the jet and by the total energy of the system takes place. At that, convergence of the first order by C is observed for ΔE (the distance between the curves at each moment of time decreases proportionally to C) and by not less than the first order by N (Figs. 2b, 2c). Convergence by velocity is slower and weakens on approaching moment t_c (Fig. 2a).

4.2. The results were compared with the computed data from [24, 25] for expansion and further contraction of a spherical cavitation bubble near a wall, when the initial pressure in the bubble p_b^0 is higher than that of the surrounding liquid p_∞ and the bubble starts contracting with the formation of a cumulative jet. The computations were performed for the following data:

$$R^* = 0.1651, \quad p_b^0/p_\infty = 100, \quad \kappa = 1.4, \quad \sigma = 0, \quad R_m = 1 \text{ mm}, \quad p_\infty = 0.1 \text{ MPa}, \quad \rho_f = 1000 \text{ kg}/\text{m}^3.$$

Figure 3 for $\gamma = 2$ shows the shapes of the bubble and the isolines of the pressure in the liquid at the end of the first motion phase at the moment $t^* = 2.128$ from the beginning of the process (Fig. 3a) and at the moment $t^* = 2.136$ in the second motion phase of the bubble (Fig. 3b). Figure 4 presents the shapes of a bubble and the isolines of pressure for $\gamma = 0.92$ in the toroidal motion phase at the moment $t^* = 2.280$. The left parts of both figures show the results of the current work, and the right parts show the results of works [24] (Fig. 3) and [25] (Fig. 4). The qualitative and quantitative correlation of the results can be observed. The bubble profiles and pressure isobars of the current work are almost identical to the ones presented in [24, 25].

4.3. The results for the bubble induced by a laser pulse in water were compared with the experimental data obtained in [26]. The following values of the initial quantities were taken for computation:

$$R^* = 0.172, \quad \kappa = 1.4, \quad \sigma = 0, \quad R_m = 1.45 \text{ mm}, \quad p_\infty = 0.1 \text{ MPa},$$

where the geometric quantities R_0, R_m, and γ are taken from [26].

Figure 5a for $\gamma = 0.9$ shows the bubble profiles at four sequential moments of time, the last of which coincides with moment t_c, when the cumulative jet touches the opposite wall of the bubble. Figure 5b for $\gamma = 2$ also presents the bubble profiles at four moments of time, the second of which coincides with the end of the first motion phase t_c. The upper rows of both Figs. 5a and 5b present the results of the current work and the lower row present the experiment results [26].

Figure 5a shows a good qualitative and quantitative agreement of the results. A comparison of the results in the toroidal motion phase (Fig. 5b, frames *3*, *4*) shows a good qualitative agreement of the bubble shapes.

5. DEMONSTRATION OF APPLICATION

The possibilities of the algorithm were demonstrated on the solution of a problem on the expansion and subsequent contraction of a spheroidal gas bubble in water at a certain distance from a wall. In partic-
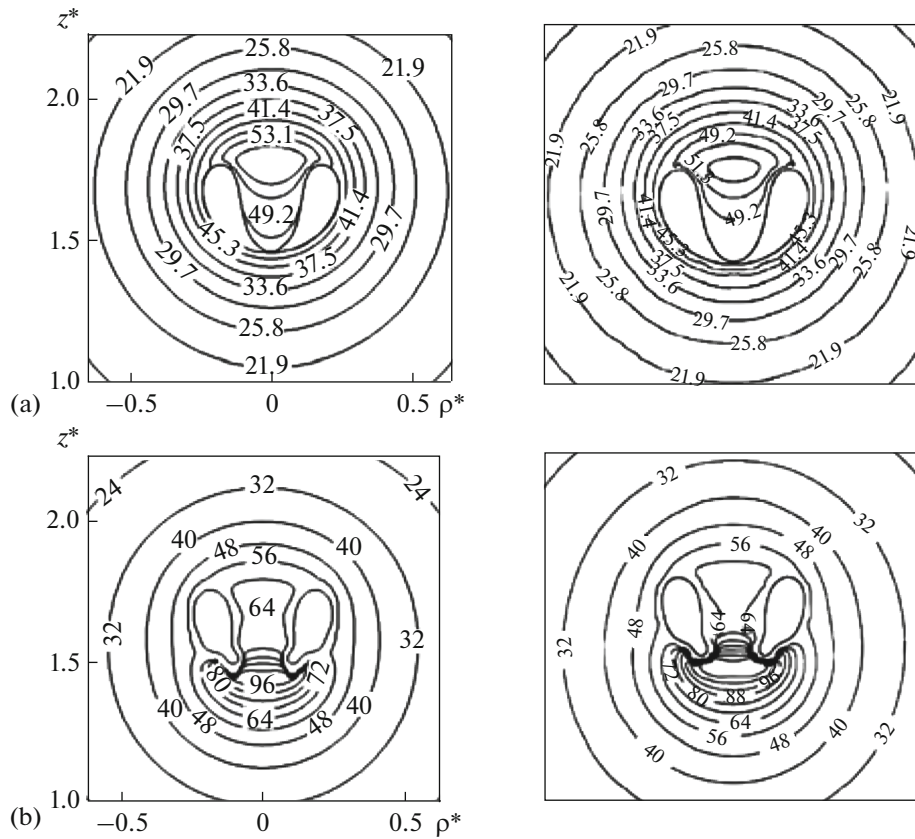
Fig. 3. Shapes of bubble and isolines of pressure (bar) at end of first motion phase ($t^* = 2.128$) of bubble (a) and at moment $t^* = 2.136$ in toroidal phase (b). On left, results of current work, on right, result of work [24].
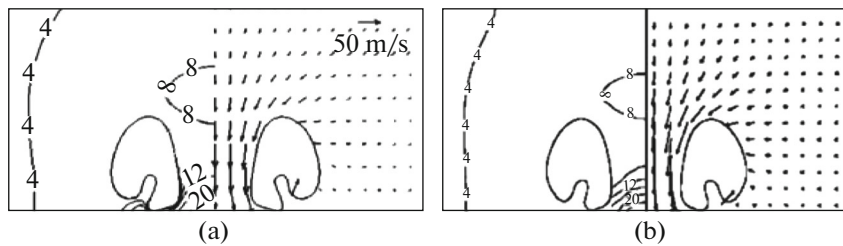
Fig. 4. Shapes of bubble, fields of pressure (bar) and velocity at moment $t^* = 2.280$ in toroidal motion phase: (a) results of current work, (b) results of work [25].

ular, expansion and contraction are realized in the case of a cavitation bubble formed by a focused laser pulse [26] or electric discharge [27] in a liquid, when a microbubble with a pressure much higher than that of the surrounding liquid appears. As a result, the bubble expands strongly and at the maximal expansion, the pressure in it is close to that of saturated vapor; then it usually contracts with the formation of a cumulative jet. The experiment allows defining the shape of the bubble relatively easily, while the velocity of the surrounding liquid is defined in a more complicated way. Numerical simulation allows estimating the effect of liquid velocity at the moment of maximal expansion on the bubble's dynamics at the subsequent contraction stage.

For this purpose we compared the results of two computational variants for an initially slightly flattened spheroidal bubble ($e = 0.8$) in water for $\gamma = 1.25$, $\kappa = 1.4$, $\sigma = 0$, $\bar{a} = 0$, $\bar{b} = 0$, and $p_\infty = 1$ bar. Variant 1 corresponds to the expansion and subsequent contraction of the bubble, whose initial volume equals the volume of a spheroidal bubble of radius $R^* = 0.1$, and the pressure in its cavity is 400 bar. Variant 2 con-
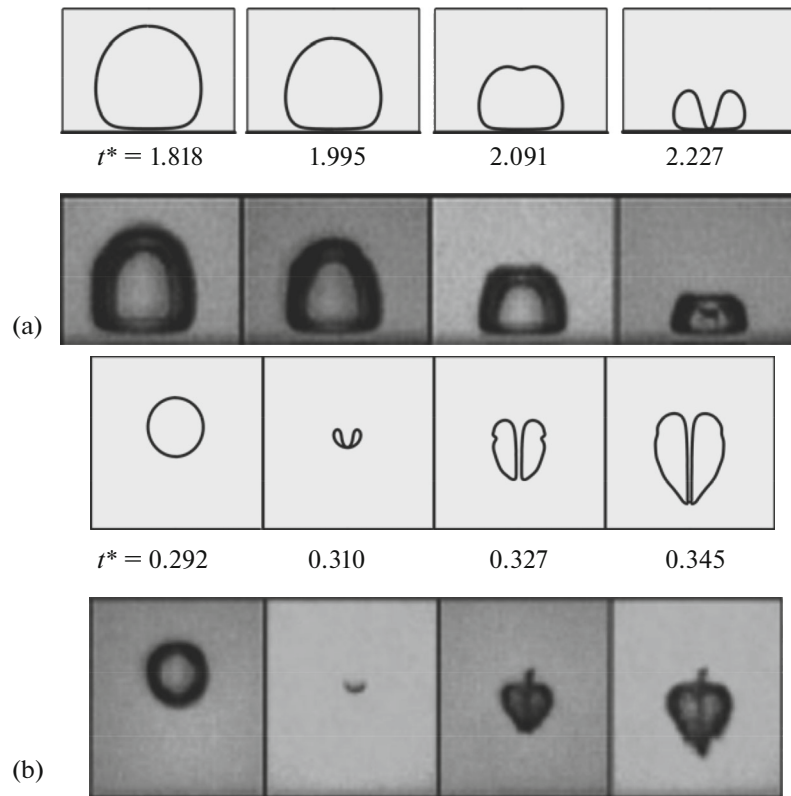
Fig. 5. Comparison of results of current work with experiments of [26] at identical moments of time: (a) in first motion phase for $\gamma = 0.9$ and (b) in first and second motion phases for $\gamma = 2.0$.

siders only the contraction of a bubble. At that, the initial shape of the bubble and the pressure in it (0.027 bar) coincide with those obtained in variant 1 at the beginning of the contraction, and liquid velocity is accepted to be zero.

The computational results are presented in Fig. 6, where Figs. 6a–6c correspond to variant 1 and Figs. 6d and 6e correspond to variant 2. Figure 6a shows the shape of the bubble, as well as the fields of the velocity and pressure of the liquid at the moment of its maximal expansion. It can be seen that the shape of the bubble is close to spherical, the maximal liquid velocity near its surface is about 1 m/s, and the pressure in the bubble corresponds to the saturation pressure. Figure 6b presents the shape of bubble, as well as the fields of the velocity and pressure of the liquid at the moment t_c. At this moment, the velocity at the end of the jet is 89.2 m/s, the maximal pressure of 17 bar is observed near the base of the jet, and pressure on the wall is approximately equal to the pressure inside the bubble (5 bar). In the toroidal phase (Fig. 6c), the shape of the bubble, as well as the fields of velocity and pressure, is given at the moment of time when the ratio between the current bubble volume V and its volume V_c at the moment t_c is 0.6. At this moment, the maximal pressure of about 55 bar is observed in the neighborhood of the part of the profile with a large curvature; at that, the pressure on the wall near the symmetry axis is 21 bar and the maximal liquid velocity on the symmetry axis is 95.4 m/s. Figure 6a shows the initial bubble shape and pressure field for variant 2. It can be seen in Fig. 6d, which presents the shape of the bubble, as well as the fields of the velocity and pressure of the liquid at the moment t_c, that the liquid velocity, the pressure in the liquid, and the pressure in the bubble are significantly higher than in variant 1. A similar picture is also observed in the toroidal phase when the volume ratio $V/V_c = 0.6$ (Fig. 6e). Figure 6f shows the pressure profiles along the radial coordinate for variants 1 and 2, when the ratio $V/V_c = 0.6$, on the wall (dashed lines), and at levels $z^* = 0.36$ (lines with black circles) and $z^* = 0.63$ (solid lines). It can be seen that at all z^* levels, the pressure in variant 1 is significantly less than in variant 2. Note that the distribution of the pressure at the levels close to the bubble surface is nonmonotonic and its maximum is observed at some distance from the axis of symmetry.
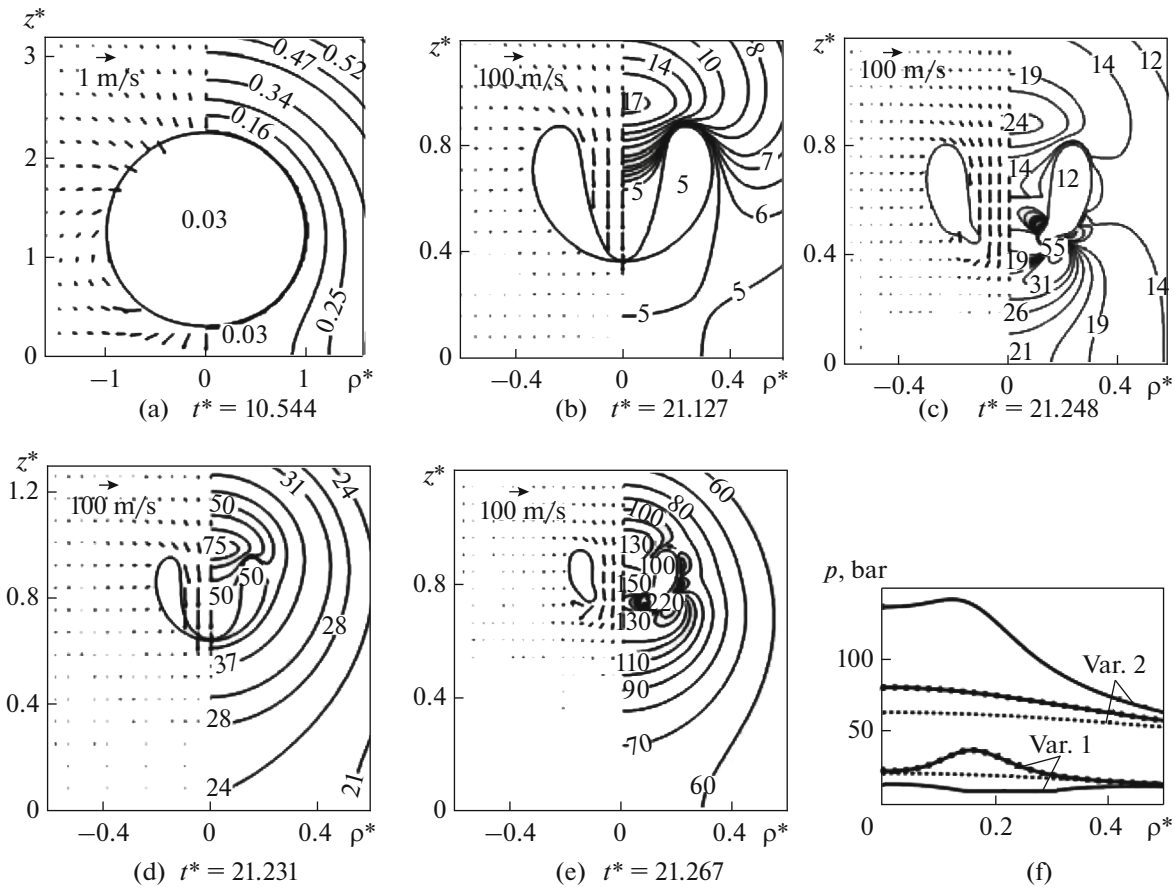
Fig. 6. Shapes of bubble, fields of velocity and pressure: (a) at maximal expansion of bubble for variant 1; (b), (d) at moment t_c; c, e in toroidal motion phase, when $V/V_c = 0.6$ for variants 1, 2; (f) pressure profiles along radial coordinate for $V/V_c = 0.6$ on wall $z^* = 0$ (dashed lines), $z^* = 0.36$ (lines with circles), and $z^* = 0.63$ (solid lines).

Thus, the results presented in Fig. 6 show that neglecting the velocity field at the end of the bubble expansion stage during the modeling of the process of expansion and subsequent contraction near the wall may lead to significant errors in the description of the contraction stage.

6. CONCLUSIONS

A numerical technique for studying the dynamics of a gas bubble in a liquid near a solid wall based on a step-by-step method in time and boundary elements method was developed. The technique consists of two stages. The first stage is for computing the dynamics of the bubble until the moment when the cumulative liquid jet formed during the contraction of the bubble on its surface hits part of the bubble surface nearest the wall. At the second stage, the dynamics of the bubble in the toroidal phase of its motion are calculated. The numerical instability against the functions defining the position of the bubble and the potential of the liquid velocity on it is eliminated with the help of smoothening using a cubical spline. The convergence of the algorithm with an increase in the number of bubble profile partitions and a refinement of the time step was shown. Comparison with the numerical and experimental results of other authors showed satisfactory agreement. The problem on expansion and subsequent contraction of the initially slightly flattened spheroidal bubble at a short distance from the wall was solved. It was shown that neglecting the liquid's motion at the end of the bubble expansion stage may lead to significant errors during the contraction stage regarding the shape of the bubble, as well as the quantities characterizing its dynamics.

ACKNOWLEDGMENTS

REFERENCES

1. V. K. Kedrinskii, *Hydrodynamics of Explosion: Experiments and Models* (Springer, 2005; Sib. Otdel. RAN, Novosibirsk, 2000).

2. M. S. Plesset and R. B. Chapman, "Collapse of an initially spherical vapour cavity in the neighbourhood of a solid boundary," J. Fluid Mech. **47**, 283−290 (1971).

3. M. Kornfeld and L. Suvorov, "On the destructive action of cavitation," J. Appl. Phys. **15**, 495−506 (1944).

4. S. Popinet and S. Zaleski, "Bubble collapse near a solid boundary: a numerical study of the influence of viscosity," J. Fluid Mech. **464**, 137−163 (2002).

5. E. Johnsen and T. Colonius, "Numerical simulations of non-spherical bubble collapse," J. Fluid Mech. **629**, 231−262 (2009).

6. C. K. Turangan and G. J. Ball, "A free-lagrange simulation of cavitation bubble collapse near a rigid boundary," in *Proceedings of the 23rd International Symposium on Shock Waves, Fort-Worth TX, USA, July 2001,* pp. 793−799.

7. O. V. Voinov and V. V. Voinov, "Numerical method of calculating non-stationary motions of ideal incompressible fluid with free surface," Sov. Phys. Dokl. **20**, 179 (1975).

8. O. V. Voinov and V. V. Voinov, "On the process of collapse of a cavitation bubble near a wall and the formation of a cumulative jet," Sov. Phys. Dokl. **21**, 133 (1976).

9. J. R. Blake, B. B. Taib, and G. Doherty, "Transient cavities near boundaries," J. Fluid Mech. **170**, 479−497 (1986).

10. Q. X. Wang, "The evolution of a gas bubble near an inclined wall," Theor. Comput. Fluid Dyn. **12**, 29−51 (1998).

11. K. E. Afanas'ev and I. V. Grigor'eva, "Numerical simulation of dynamics of spatial vapour-gas bubbles," Vych. Tekhnol. **11** (Spec. Iss.), 4−25 (2006).

12. J. P. Best, "The formation of toroidal bubbles upon the collapse of transient cavities," J. Fluid Mech. **251**, 79−107 (1993).

13. A. Pearson, J. R. Blake, and S. R. Otto, "Jets in bubbles," J. Eng. Math. **48**, 391−412 (2004).

14. S. Zhang, J. H. Duncan, and G. L. Chahine, "The final stage of the collapse of a cavitation bubble near a rigid wall," J. Fluid Mech. **257**, 147−181 (1993).

15. Q. X. Wang, K. S. Yeo, B. C. Khoo, and K. Y. Lam, "Nonlinear interaction between gas bubble and free surface," Comput. Fluids **25**, 607−628 (1996).

16. M. Lee, E. Klaseboer, and B. C. Khoo, "On the boundary integral method for the rebounding bubble," J. Fluid Mech. **570**, 407−429 (2007).

17. J. P. Best, "The rebound of toroidal bubbles," in *Bubble Dynamics and Interface Phenomena* (Kluwer Academic, Dordrecht, 1994), pp. 405−412.

18. Z. Y. Zhang and H. S. Zhang, "Surface tension effects on the behavior of a cavity growing, collapsing and rebounding near a rigid wall," Phys. Rev. E **70**, 056310 (2004).

19. A. A. Aganin, M. A. Il'gamov, L. A. Kosolapova, and V. G. Malakhov, "Collapse of a cavitation bubble in fluid near rigid wall," Vestn. Bashkir. Univ. **18** (1), 15−21 (2013).

20. A. A. Aganin, M. A. Il'gamov, L. A. Kosolapova, and V. G. Malakhov, "Dynamics of cavitation bubble near a solid wall," Thermophys. Aeromech. **23**, 211−220 (2016).

21. L. A. Kosolapova and V. G. Malakhov, "Numerical study of dynamics of spheroidal cavitation bubbles near rigid wall," in *Grid Methods for Boundary Problems and Applications, Proceedings of he 10th International Conference, Kazan', Sept. 24−29, 2014* (Kazan. Univ., Kazan, 2014), pp. 429−434.

22. C. A. Brebbia, J. C. F. Telles, and L. C. Wrobel, *Boundary Element Techniques: Theory and Applications in Engineering* (Springer, Berlin, Heidelberg, 1984).

23. J. P. Best and A. Kucera, "A numerical investigation of non-spherical rebounding bubbles," J. Fluid Mech. **245**, 137−154 (1992).

24. J. P. Best, "The dynamics of underwater explosions," PhD Thesis (The Univ. Wollongong, Australia, 1991).

25. R. P. Tong, W. P. Schiffers, S. J. Shaw, J. R. Blake, and D. C. Emmony, "The role of `splashing' in the collapse of a laser-generated cavity near a rigid boundary," J. Fluid Mech. **380**, 339−361 (1999).

26. A. Philipp and W. Lauterborn, "Cavitation erosion by single laser-produced bubbles," J. Fluid Mech. **361**, 75−116 (1998).

27. Y. Tomita and A. Shima, "Mechanisms of impulsive pressure generation and damage pit formation by bubble collapse," J. Fluid Mech. **169**, 535−564 (1986).

Translated by K. Gumerov